The Circulation of the World Ocean: A Numerical Study. Part I, A Homogeneous Model

KIRK BRYAN AND MICHAEL D. COX

Geophysical Fluid Dynamics Laboratory, NOAA, Princeton University, Princeton, N. J. 08540

(Manuscript received 1 April 1972, in revised form 5 June 1972)

ABSTRACT

Calculations are carried out for a homogeneous model of the World Ocean. Solutions for the large-scale, wind-driven circulation are obtained by numerical integration with respect to time of a numerical model. The model includes 9 levels in the vertical and has a horizontal resolution of $2°\times2°$ in latitude and longitude. Subgrid-scale motions are included implicitly through the eddy viscosity hypothesis. The level of viscosity is adjusted so that only scales of motion large enough to be resolved by the numerical model will have appreciable amplitude. Compared with available observations, the model with uniform depth tends to underpredict the strength of the transport in the Northern Hemisphere boundary currents, but overpredict the strength of the Antarctic Circumpolar Current and the East Australian Current. When bottom topography is taken into account, the Northern Hemisphere transport patterns are not greatly altered, but transport of the Antarctic Circumpolar Current and the East Australian Current are drastically reduced.

1. Introduction

Analysis of water mass data and measurements of radioactive tracers indicate that the circulations of the deep water of all the major oceans are very closely tied together. In considering the large-scale ocean circulation and interaction of the atmosphere and the ocean on a global scale, a model of the entire World Ocean is needed. For such a model to be useful it must provide for at least a minimal resolution of all the major ocean currents and be fully three-dimensional. There must be sufficient vertical resolution to specify the thermocline and other large-scale features of the water mass structure. For the purpose of extending the climatic calculations with a joint air-sea model, the global ocean model should be capable of simulating, with some accuracy, the transfer of heat by ocean currents from tropical to polar latitudes.

There is an interesting analogy between a model for large-scale ocean circulation studies and a turbulence calculation. To reduce the total degrees of freedom to a manageable number, we must restrict our attention to a space-averaged form of the equations of motion which correspond to the familiar Reynolds equations. Only the space-averaged variables can be treated explicitly. The interaction with smaller scales of motion is represented by Reynolds stresses which must be specified by a closure hypothesis. In the present study we use the turbulent viscosity approximation as a simple linear closure scheme, but in the future, observation programs like MODE (Mid-Ocean Dynamics Experiment) may provide the empirical basis for more accurate closure schemes.

The present model allows for 9 levels in the vertical plane and over 10,000 degrees of freedom for each variable in the horizontal plane. Although this number seems large, it is still necessary to average over blocks of the World Ocean several hundreds of kilometers in each horizontal dimension and of the order of hundreds of meters in the vertical direction. The level of turbulent viscosity in the closure scheme is not a parameter entirely at our disposal. A minimum level of viscosity is required so that motions with space scales less than the limit of resolution of the numerical grid will damp out rapidly, relative to the advective time scale for ocean circulation. In other words, the model ocean must be viscous enough so that the range of wavenumbers with significant amplitude does not exceed the range of wavenumbers that can be represented by the numerical solution. Otherwise, accurate numerical solutions cannot be obtained. In one sense it may be premature to attempt to model the World Ocean until we can deal with systems with larger numbers of degrees of freedom. However, computations in the parameter range that is accessible to us should provide a logical basis for extending ocean circulation studies to higher Reynolds numbers as more powerful computers become available.

Due to the complexity of the calculation, it appears best to proceed in a step-by-step fashion. In the present paper (Part I) only the outline of the method and the results for the homogeneous case will be included. Consideration of the baroclinic case will be deferred to Part II, while calculations with a joint air-sea global model will be taken up in separate

investigations. The homogeneous density case provides a very good test of the behavior of the model, since it allows a comparison with familiar analytic results from the theory of wind-driven oceans [see Stommel's, *The Gulf Stream* (1958) for a review]. In the case of uniform depth, there are also several other recently published numerical solutions for the World Ocean which are available for comparison (Sag, 1969; Il'in *et al.*, 1969; Takano, 1969). The case of a homogeneous ocean with nonuniform depth has been considered by Leichtmann *et al.* (1971). In agreement with their results, it will be shown that topography greatly alters the solution of a model of a homogeneous, wind-driven world ocean relative to the uniform depth case.

2. Equations of the model

The basic formulation of the model is similar to that given in Bryan (1969) and Cox (1970). The Navier-Stokes equations for a rotating spherical geometry have been modified in several important respects. First, density differences are neglected except in the buoyancy term, i.e., the Boussinesq approximation is made. Second, the local acceleration and other terms of the same order are neglected in the equation of motion for the vertical component, reducing it to the hydrostatic approximation. Third, only the large-scale motion is treated explicitly, while the stresses exerted by smaller scales are treated implicitly. Due to the very large scales considered, ordinary viscosity and conductivity are negligible and are consequently neglected.

Let

$$\left.\begin{aligned} m&=\sec\varphi \\ n&=\sin\varphi \\ u&=a\dot{\lambda}m^{-1} \\ v&=a\dot{\varphi} \end{aligned}\right\}.$$

The equations of motions for u and v are

$$u_t-2\Omega nv=-\frac{m}{a}(p/\rho_0)_\lambda+G^\lambda, \tag{1}$$

$$v_t+2\Omega nu=-\frac{1}{a}(p/\rho_0)_\varphi+G^\varphi, \tag{2}$$

where the angular velocity of the earth is designated by Ω, while ρ and ρ_0 are pressure and the average density, respectively; and

$$G^\lambda=-\frac{m}{a}[(u^2)_\lambda+(uv/m)_\varphi]-(wu)_z+mnuv/a+A_v u_{zz} +A_m a^{-2}[\Delta u+(1-m^2n^2)u-2nm^2v_\lambda], \tag{3}$$

$$G^\varphi=-\frac{m}{a}[(uv)_\lambda+(v^2/m)_\varphi]-(wv)_z-mnu^2/a+A_v v_{zz} +A_m a^{-2}[\Delta v+(1-m^2n^2)v+2nm^2u_\lambda], \tag{4}$$

$$\Delta=m^2(\ )_{\lambda\lambda}+m[(\ )_\varphi m^{-1}]_\varphi. \tag{5}$$

The advective terms in the momentum equations are cast in conservative form. A_v and A_m are constant "eddy viscosity" coefficients in the vertical and horizontal directions, respectively.

The hydrostatic relation is

$$\rho g=-p_z \tag{6}$$

and the continuity equation

$$w_z+\frac{m}{a}[u_\lambda+(v/m)_\varphi]=0. \tag{7}$$

In Part I, density is simply treated as a constant everywhere in the World Ocean, while in Part II it will be specified as a function of λ, φ and z from observation. Therefore, no prediction equations are needed for the determination of the temperature and salinity fields.

At the lateral walls the boundary conditions on u, v are

$$u, v=0.$$

Since the principle goal of the calculation is to investigate the mean average ocean circulation, we adopt the "rigid-lid" approximation which filters out external inertia-gravitational oscillations. With this approximation, the kinematic effect of variations of the position of the upper surface of the ocean are neglected, i.e., at $z=0$,

$$\left.\begin{aligned} w&=0 \\ \rho_0 A_v(u_z,v_z)&=\tau^\lambda,\tau^\varphi \end{aligned}\right\}. \tag{8}$$

At the lower boundary ($z=-H$)

$$w(-H)=-ua^{-1}mH_\lambda-va^{-1}H_\varphi, \tag{9}$$

$$\rho_0 A_v(u_z,v_z)=(\Omega A_v\sin\varphi)^{\frac{1}{2}}\rho_0[(u\mp v),(v\pm u)]. \tag{10}$$

At the upper surface the stress is specified from climatological data and at the lower boundary it is calculated from Ekman theory. This approach avoids the necessity for a detailed calculation of velocity profiles in the bottom Ekman layer. In (10) the upper and lower signs refer to the Northern and Southern Hemisphere, respectively.

Relations (1)–(6) form a complete description of the model, but further manipulation is required to obtain the form of the equations which serve as the basis for the numerical model. In order to eliminate pressure (1) and (2) are differentiated with respect to z to yield

$$u_{tz}-2\Omega nv_z=-\frac{m}{a}g\rho_\lambda\frac{1}{\rho_0}+(G^\lambda)_z, \tag{11}$$

$$v_{tz}+2\Omega nu_z=-\frac{1}{a}g\rho_\varphi\frac{1}{\rho_0}+(G^\varphi)_z. \tag{12}$$

Integrating the continuity equation (7), we have

$$w(0)-w(-H)=-\frac{m}{a}\left[\left(\int_{-H}^{0} u\,dz\right)_\lambda+\left(\int_{-H}^{0} vm^{-1}dz\right)_\varphi -u(-H)H_\lambda-vm^{-1}(-H)H_\varphi\right]. \quad (13)$$

Making use of the boundary conditions (8) and (9), we see that it is possible to obtain a transport streamfunction,

$$\psi_\lambda,\psi_\varphi=m^{-1}a\int_{-H}^{0}\rho_0 v\,dz,\ -a\int_{-H}^{0}\rho_0 u\,dz. \quad (14)$$

Taking the vertical integral of (1) and (2) and making use of the hydrostatic relation, we obtain

$$\frac{1}{a}(-\psi_{\varphi t}-2\Omega mn\psi_\lambda) =-\frac{mH}{a}(p^s)_\lambda+\int_{-H}^{0}\left(\rho_0 G^\lambda-a^{-1}\int_z^0 mg\rho_\lambda dz'\right)dz, \quad (15)$$

$$\frac{1}{a}(m\psi_{\lambda t}-2\Omega n\psi_\varphi) =-\frac{H}{a}(p^s)_\varphi+\int_{-H}^{0}\left(\rho_0 G^\varphi-\int_z^0 ga^{-1}\rho_\varphi dz'\right)dz. \quad (16)$$

In (15) and (16) p^s is the surface pressure. While density can be measured directly, p^s cannot. To eliminate this term, (15) and (16) are divided by H and cross-differentiated to form a single transport vorticity equation:

$$a^{-1}(m\psi_{\lambda t}H^{-1})_\lambda+a^{-1}[\psi_{\varphi t}(mH)^{-1}]_\varphi =\left[\frac{2\Omega n}{a}\psi_\varphi H^{-1}+H^{-1}\int_{-H}^{0}\left(\rho_0 G^\varphi-\int_z^0 ga^{-1}\rho_\varphi dz'\right)dz\right]_\lambda -\left[\frac{2\Omega n}{a}\psi_\lambda H^{-1}+(mH)^{-1} \times\int_{-H}^{0}\left(\rho_0 G^\lambda-\int_z^0 gma^{-1}\rho_\lambda dz'\right)dz\right]_\varphi. \quad (17)$$

The boundary condition corresponding to the case of no normal flow at the boundaries is simply that the boundaries coincide with a streamline. The relations (11) and (12) predict the shape of the velocity profile, and (17) predicts a reference velocity by specifying the total integrated transport.

One complication in the transport streamfunction formulation is due to the existence of isolated continents and large islands. All boundaries coincide with streamlines, but a changing net circulation can occur around islands. A method for doing this is given by Kamenkovich (1962) and its extension to the time-dependent problem is outlined in Bryan (1969). However, the numerical method for islands given in Bryan (1969) proved to be unsatisfactory in the general case of nonuniform bottom topography. The modified numerical procedure[1] used in the present calculation is shown in the Appendix.

3. Finite-difference formulation

A detailed description of the finite-difference method as well as a discussion of its important properties is given in Bryan (1969), but in order to eliminate reference to that paper, a concise outline of the numerical method will be given here. Readers who are primarily interested in results rather than the method of solution should proceed directly to Section 4.

It is convenient to think of the horizontal arrangement of variables in terms of a checkerboard pattern. The transport streamfunction and the density are defined at the center of squares and both velocity components are specified at corners of the squares. Let us define two finite difference operators

$$\delta_\lambda g=(g_{i+\frac{1}{2}}-g_{i-\frac{1}{2}})(a\Delta\lambda)^{-1}, \quad (18)$$

$$\bar{g}^\lambda=0.5(g_{i+\frac{1}{2}}+g_{i-\frac{1}{2}}). \quad (19)$$

Similar operators may be defined for the half-integer points and also in the φ and z directions.

Let K_{mx} be the total number of levels at any one position. In general, K_{mx} will vary widely from one point to another depending on the total depth. The relationship between the velocity components and the transport streamfunction given in (14) may be written

$$\delta_\lambda\bar{\psi}^\varphi,\delta_\varphi\bar{\psi}^\lambda=\sum_{k=1}^{K_{mx}}\rho_0(m^{-1}v,\ -u)\Delta_k. \quad (20)$$

Let the superscript l indicate the time step level. In this case

$$\delta_l\bar{g}^t=(g^{l+1}-g^{l-1})(2\Delta t)^{-1}. \quad (21)$$

The finite-difference equivalent to (11) is

$$\delta_z[\delta_l\bar{u}^t-2\Omega n_j(\tfrac{2}{3}v^{l+1}+\tfrac{1}{3}v^{l-1})-G^\lambda]=gm_j\delta_\lambda\bar{\rho}^{\varphi z}\rho_0^{-1}, \quad (22)$$

where

$$-G^\lambda=m_j\delta_\lambda(\bar{u}^\lambda U)+m_j\delta_\varphi(\bar{u}^\varphi V)+\delta_z(\bar{u}^z W) -m_j n_j uv(a^{-1})-A_v\delta_z\delta_z u -A_H\{m_j^2\delta_\lambda\delta_\lambda u+m_j\delta_\varphi(m_j^{-1}\delta_\varphi u) +[1-(m_jn_j)^2]u-2m_j^2n_j\delta_\lambda\bar{v}^\lambda\}. \quad (23)$$

In (22) the reader should note that the Coriolis term

[1] It has been pointed out by K. Takano (personal communication) that a technique called "hole relaxation" can also be used to handle islands (Allen, 1954). Although slightly less efficient than the method outlined in the Appendix, "hole relaxation" should be easier to formulate in a working program.

is evaluated at $l+1$ and $l-1$ time steps rather than at the lth time step. This implicit formulation allows a longer time step in certain circumstances. The finite-difference form of the equation to predict $\delta_z v$ is exactly parallel to (22) and (23) and will therefore not be written here. The finite-difference form of the continuity equation at u, v points is

$$m^{-1}\delta_z W+\delta_\lambda U+\delta_\varphi V=0, \tag{24}$$

where

$$U=\bar{u}^\lambda+(\overline{H^{-1}\delta_\varphi\bar{\psi}^\lambda}^\lambda-H^{-1}\delta_\varphi\psi)\rho_0^{-1}, \tag{25}$$

$$V=\overline{v\cos\varphi}^\varphi-(\overline{H^{-1}\delta_\lambda\bar{\psi}^\varphi}^\varphi-H^{-1}\delta_\lambda\psi)\rho_0^{-1}. \tag{26}$$

The particular form of (20), (24), (25) and (26) insures that the finite difference equivalent of (8) and (9) are satisfied.

The transport vorticity equation has the form

$$\delta_t\overline{\{\delta_\lambda(mH^{-1}\delta_\lambda\psi)+\delta_\varphi[(mH^{-1})\delta_\varphi\psi]\}}^t=\delta_\lambda\bar{N}^\varphi-\delta_\varphi\bar{M}^\lambda, \tag{27}$$

where

$$N=H^{-1}\Big[2\Omega n_j\delta_\varphi\bar{\psi}^\lambda+\sum_{k=1}^{K_{mx}}(\rho_0 G^\varphi-\sum_{k'=1}^{k}g\delta_\varphi\bar{\rho}^\lambda\Delta_{k'})\Delta_k\Big], \tag{28}$$

$$M=(Hm_j)^{-1}\Big[2\Omega n_j m_j\delta_\lambda\bar{\psi}^\varphi+\sum_{k=1}^{K_{mx}}(\rho_0 G^\lambda-\sum_{k'=1}^{k}gm_j\delta_\lambda\bar{\rho}^\varphi\Delta_{k'})\Delta_k\Big]. \tag{29}$$

4. Layout of the finite-difference numerical grid

A familiar difficulty in finite-difference calculations for a sphere is that any regular projection of the surface of a sphere will contain a singularity. The singularity itself does not cause so much difficulty as the clustering of coordinate lines in the vicinity. In the case of a numerical integration with respect to time, the maximum time step is limited by the Courant-Friedrichs-Lewy stability criterion. The time step is limited by the distance between grid points. In regions near a singularity, a very short time step would be required, resulting in an inefficient calculation for the grid as a whole.

To avoid this problem in the present calculation, the entire area of the World Ocean is represented by three different grids. The largest area is covered by a central grid based on spherical geometry. Grid points are placed at intersections of meridians and lines of constant latitude. The grid is centered along the equator and extends to 62° north and south. Separate spherical grids are used for the polar regions. On the polar grids, the equator line corresponds to a meridian of the central grid and runs through the pole. Correspondingly, the polar point of the polar grids lies along the equator of the central grid, based on true latitude and longitude.

Due to the different distribution of land and sea in the two hemispheres, the two polar grids are somewhat different. At the north pole, the equator of the new grid coincides with 25W longitude. The grid covers a 62° span of longitude and a 38° span of latitude. The long axis of this rectangular domain extends down into the North Atlantic from the Arctic Ocean. The grid at the south pole is more symmetric. It covers an 84°×84° span of latitude and longitude and its equatorial line corresponds to 105W longitude. The three grids are shown in Fig. 1. Note that they overlap to a considerable degree. Some redundancy arises since calculations are carried out twice in the overlapping regions. This feature, however, seems to minimize the normal difficulties of joining two different grids together.

In integrating the equations of the model, calculations are carried out separately for each grid over a specified number of time steps amounting to some fraction of a day. Boundary conditions along open boundaries consist of ψ values interpolated from the adjacent grid. No attempt is made to prescribe the details of the velocity profile at the open boundaries. Instead, we set

$$\frac{\partial}{\partial n'}\Big[(u,v)-\frac{1}{H}\int_{-H}^{0}(u,v)dz\Big]=0. \tag{30}$$

Here n' is the coordinate normal to the open boundary in question. For the highly geostrophic flow of the World Ocean, flow tends to be independent of height except in planetary boundary layers. If the total transport and wind stress is given, the velocity profiles in the planetary boundary layers are locally determined. Therefore, (30) is a sufficient condition for large-scale flow.

5. Parameters of the model

A lattice spacing of 2°×2° of latitude and longitude is the finest spacing possible with the computing equipment available to the authors. Near the equator this resolution is equivalent to a square mesh with 220 km between mesh points. As will be apparent later, this resolution limits us to the consideration of the viscous range in which inertial effects play an almost insignificant role in the momentum balance. Until more powerful computers become available, nonlinear regions at lower Ekman numbers can only be calculated for limited areas of the ocean with observed or computed inflow conditions on the open boundaries.

The three-dimensional model has 9 layers. The total depth for each vertical column is chosen to correspond to the lower interface of that particular layer which is closest to the actual depth given by Scripps compilation of the elevation of the earth's surface (Lee and Kaula, 1967). The 9 discrete depths that are

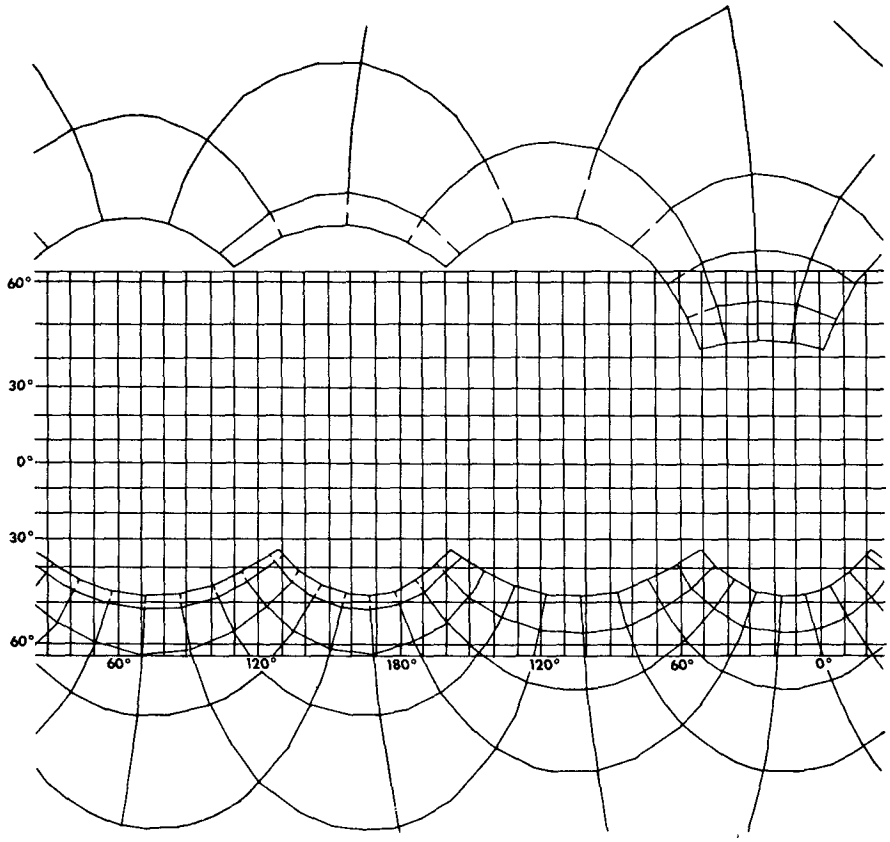

FIG. 1. The layout of the three grids used to cover the area of the World Ocean. The actual network is much denser than that shown.

allowed in the model are as follows:

Level	Depth (m)
1	42
2	90
3	257
4	555
5	1164
6	2131
7	3358
8	4741
9	6186

It should be mentioned that the model is more general than it need be for the choice of parameters (homogeneous case, viscous range) considered here. Except for details near the equator, essentially the same results could be obtained using a vertically integrated model rather than a three-dimensional model (see Greenspan, 1968, pp. 225–233 for a discussion of this). In the present study, the use of a more general formulation is justified by the fact that we wish to use the same model but include the effect of baroclinicity in Part II. The model parameters are given in Table 1.

In the baroclinic case, the three-dimensional structure of the circulation will become of critical importance. In order to compare the homogeneous and baroclinic cases, it is desirable to use the same set of equations and finite-difference schemes in both cases.

To facilitate the discussion, it is convenient to define horizontal and vertical Ekman numbers, where

$$\mathrm{Ek}_H = \frac{A_M}{\Omega a^2},$$

$$\mathrm{Ek}_V = \frac{A_V}{\Omega H^2}.$$

The Ekman number expresses the ratio of the viscous terms to the Coriolis terms in the equations of motion and replaces the Reynolds number as the primary measure of viscous effects of a rotating fluid. A detailed

TABLE 1. Parameters of the model and the scale thickness of the western boundary current and the surface flow layer.

t	Time step	0.375×10^{4} sec
a	Radius of the earth	6.37×10^{8} cm
H	Depth	5×10^{5} cm
Ω	Angular velocity	0.72919×10^{-4} sec^{-1}
A_M	Horizontal mixing coefficient	4×10^{8} cm^2 sec^{-1}
A_V	Vertical mixing coefficient	1.0 cm^2 sec^{-1}
Ek_H	Ekman number (horizontal)	1.33×10^{-5}
Ek_V	Ekman number (vertical)	5.49×10^{-8}
$(\mathrm{Ek}_H)^{\frac{1}{2}}a$	Boundary layer thickness	324 km
$(\mathrm{Ek}_V)^{\frac{1}{2}}H$	Ekman layer thickness	1.16 m
$a(\Delta\varphi,\Delta\lambda)$	Grid point interval	220 km

analysis of the lateral boundary layer structure, in the case of a model based on the complete Navier-Stokes equations, has been made by Robinson (1970). The present model is hydrostatic, and is therefore not capable of reproducing all the details indicated in Robinson's analysis. As a minimum requirement, however, the numerical model should include the Munk (1950) viscous boundary layer. A measure of the Munk layer is $Ek_H^{\frac{1}{3}}a$. As indicated in Table 1, the parameters used in the computations give a value of slightly over 300 km for the Munk layer. In reality, the western boundary currents of the Northern Hemisphere are narrower by a factor of 5. Limitations of computer capacity, however, do not allow us to compute a solution for the entire World Ocean and simultaneously include smaller scale features of the major currents.

One of the peculiarities of rotating flows is that the vertical Ekman layers on upper or lower boundaries are quite different from the side-wall layers. Under steady conditions and low Rossby number, it is possible to compute the stress at the boundary from the free flow outside of the layer. This allows us to include the planetary friction layers implicitly without resolving the details of the Ekman spiral. This point is discussed in more detail by Bryan and Cox (1968). Note that the choice of a vertical mixing coefficient only influences the stress due to bottom friction, since the stress at the upper surface is specified *a priori*.

The specified wind-stress pattern is shown in Fig. 2. It is based on tables prepared by Hellerman (1967) but extended to polar latitudes by the authors. The pattern of Fig. 2 represents the annual mean wind

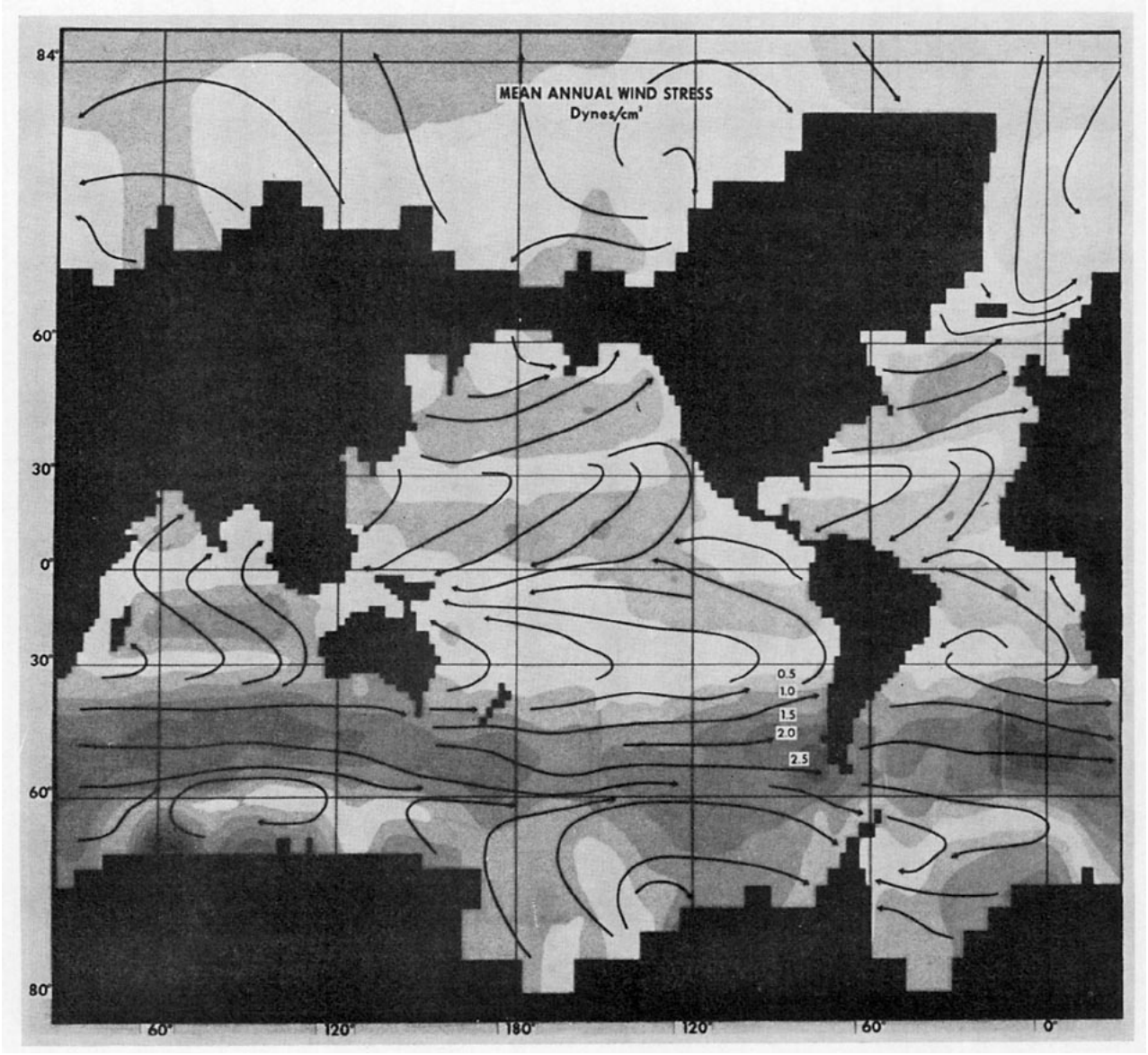

FIG. 2. Annual mean wind-stress field after Hellerman (1967) but extended to the poles. Units are dyn cm^{-2}.

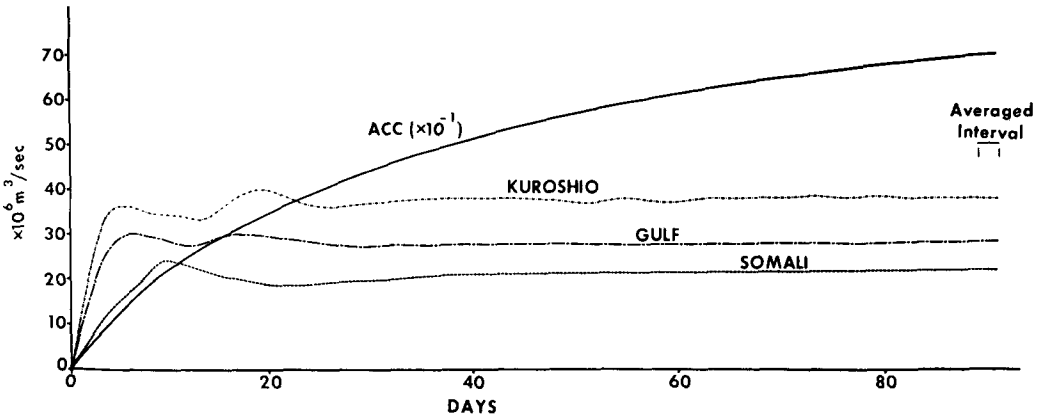

FIG. 3. Time-dependent behavior of the total transport of the Antarctic Circumpolar Current (ACC) and the major gyres. Note that ACC is an order of magnitude larger than the other values. A_M is equal to 4×10^8 cm^2 sec^{-1}.

stress based on wind-rose data given in U. S. Navy atlases.

6. Results of the calculations

The method of finding solutions is similar to that used in previous numerical ocean circulation studies (Bryan and Cox, 1968). Starting from a state of rest, an initial value problem is solved by numerical integration with respect to time. For the case of homogeneous density, the adjustment is rather rapid. The response with respect to time is shown in Fig. 3. The transports of the western boundary currents attain their peak value within a few days. The final values correspond closely to wind-driven ocean theory, but are, of course, much less than what are actually observed (Stommel, 1958). In the Northern Hemisphere the response time is essentially the time required for a Rossby wave to traverse the basin. Subsequent oscillations die out rather quickly for the rather viscous regime considered here. In the Southern Hemisphere the situation is somewhat different due to the break in land barriers at the Drake Passage.

As pointed out by Munk and Palmén (1951) the circumpolar current must accelerate until the westerly momentum fed in by the wind is balanced by corresponding losses of momentum. In the present calculation, bottom friction is very small so that the wind torque must be balanced almost entirely by lateral friction, mainly in the vicinity of the Drake Passage. In Fig. 3 it should be noted that the transport of the circumpolar current is still increasing after 90 days, when the run is terminated. It appears that a full equilibrium would not be achieved until the integration is carried out for at least twice that time interval. The long response time may be explained qualitatively on the basis of the diffusion time for momentum. Let us assign a value of 1000 km to the width of the Drake Passage. If this width is given by δ, the diffusion time is $\delta^2/A_M \approx 250$ days.

Compared to existing estimates based on actual data, the indicated transport of the circumpolar current is extremely large. At 90 days the transport exceeds 600×10^6 tons sec^{-1} and is still increasing. In the real ocean, currents usually have their maximum value at the surface and decrease with increasing depth. The Drake Passage is approximately 1000 km wide and 4 km deep. To obtain a transport as high as 600×10^6 tons sec^{-1} would require that the observed surface currents of 20 cm sec^{-1} extend all the way to the bottom without any attenuation. Recent measurements of transport through the Drake Passage have led to ambiguous results. Combined current meter and geostrophic calculations made by Reid and Nowlin (1971) indicated a value of 237×10^6 tons sec^{-1}. On the other hand, unpublished measurements[2] by the Bedford Institute of Canada using the same methods indicate a transport near zero.

The pattern of the mass transport streamfunction shown in Fig. 4 corresponds to a two-day average of the solution after 90 days of numerical integration of the uniform depth model. The patterns may be compared to a pioneering calculation for the same case by Sag (1969) shown in Fig. 5. The wind-stress pattern is the same in both cases, but the lateral viscosity is actually one order of magnitude less in Sag's model. The Northern Hemisphere gyres have nearly the same amplitude in both cases, but it is surprising that the width of the western boundary currents in Fig. 5 is actually greater than in Fig. 4. This discrepancy may be associated with Sag's use of first-order space differencing rather than the more accurate second-order differencing. Differences in the Southern Hemisphere between the two patterns are largely due to a different treatment of the circumpolar current. In Sag's (1969) model the transport is specified *a priori* to a value of 150×10^6 tons sec^{-1}. In the present model, the trans-

[2] Personal Communication by C. R. Mann, Atlantic Oceanographic Laboratory, Dartmouth, Nova Scotia, 1971.

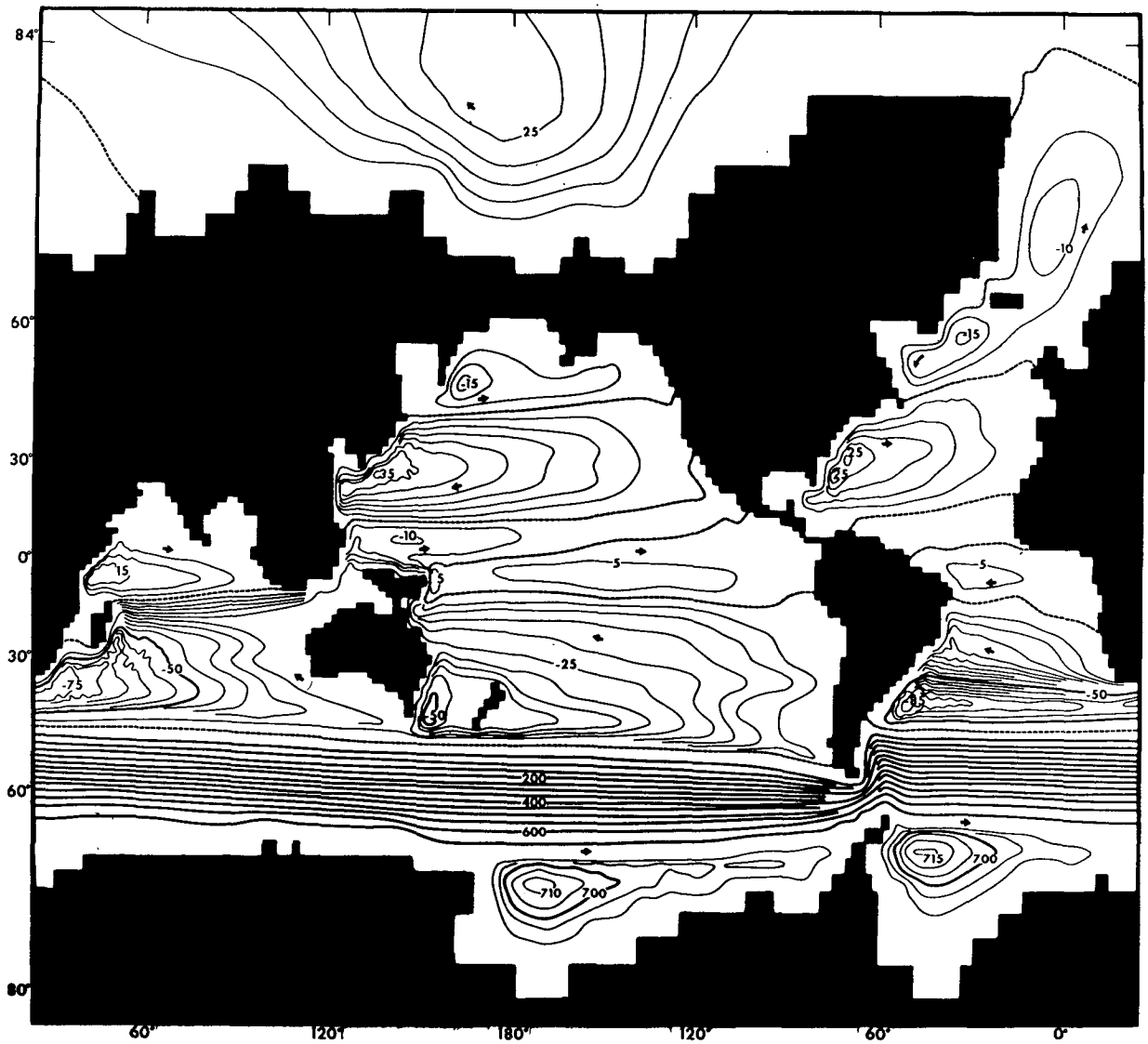

FIG. 4. Transport streamlines for the case of uniform depth, homogeneous density and wind-stress values given by Hellerman (1967). units are 10^6 tons sec^{-1}. A_M is equal to 4×10^8 cm^2 sec^{-1}.

port is calculated by the method outlined in the Appendix. It is apparent that some vorticity diffuses from the circumpolar current region to the adjacent gyres, since the Southern Hemisphere subtropical gyres slowly increase in amplitude as the circumpolar current transport increases during the numerical integration. Other calculations of this type by Takano (1969) and Il'in *et al.* (1969) indicate similar patterns in the interior regions, but differ in the vicinity of western boundary currents and the circumpolar currents. Takano's calculation is carried out with 5°×5° grid, which only allows a very crude resolution of the flow. The calculation by Il'in *et al.* is more detailed. The explicit frictional mechanism in their model is bottom friction. For the parameters considered, quite a reasonable transport through the Drake Passage is obtained.

Next, we consider the effects of introducing bottom topography into the model. For idealized inviscid flow in a homogeneous rotating fluid, the vertical component of potential vorticity is conserved along trajectories. Let ζ be the vertical component of relative vorticity, then

$$\text{Potential vorticity}=H^{-1}(\zeta+2\Omega\sin\varphi). \qquad (31)$$

For a low Rossby number, the contribution of ζ is relatively unimportant and flow will be guided along lines of constant $H\csc\varphi$. Gill and Parker (1970) have published an interesting chart of $H\csc\varphi$ for the World Ocean based on the depth values given by Lee and Kaula (1967). In Fig. 6 a similar chart is shown based on the depth configuration actually used in the present model. There is some distortion introduced since the model only allows for the nine discrete values of depth

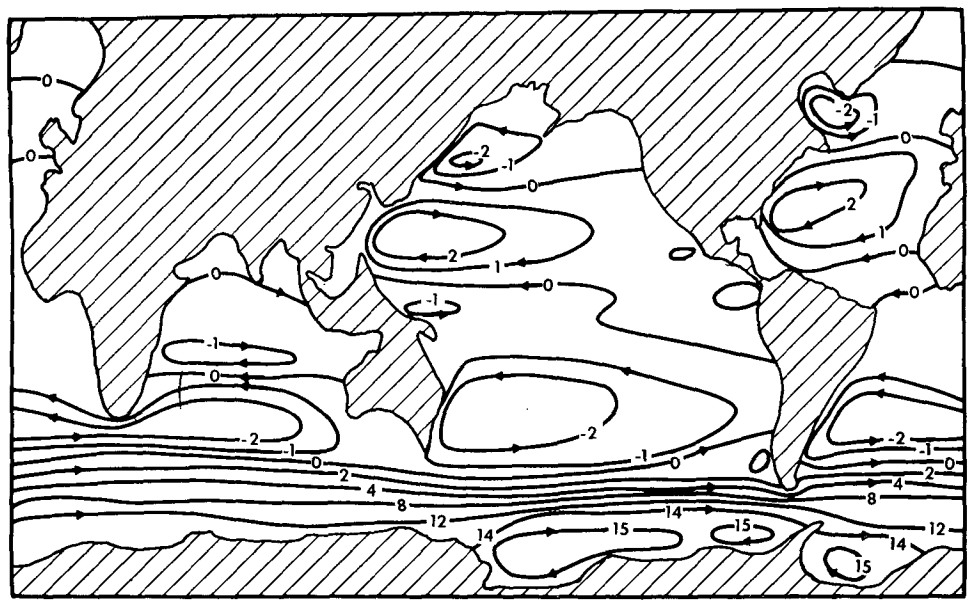

FIG. 5. Transport streamlines calculated by Sag (1969). The wind-stress distribution is the same as that in Fig. 3. Units are 10^7 tons sec^{-1}.

given in Section 5. Although many details are left out, major features such as the Mid-Atlantic Ridge, the East Pacific Rise and the island arcs of the Southwest Pacific can be recognized.

A very recent result obtained by Leichtmann *et al.* (1971) is shown in Fig. 7. The model is similar to that of Il'in *et al.*, but includes bottom topography, inertial terms and time dependence. The resolution is 5°×5°. Comparing the transport patterns shown in Figs. 3 and 4, the most significant differences are in the Southern Hemisphere. In particular, the circumpolar current is no longer zonal and there is no longer a western boundary current off of Australia. The circumpolar current is intense in the vicinity of the Macquarie Ridge, south of Australia, and in the vicinity of the Drake Passage. At other longitudes it tends to be much more diffuse. On the basis of the annual average wind distribution, the transport through the Drake Passage is calculated to be 325×10^6 tons sec^{-1}.

Calculations for the same case with the present model are shown in Fig. 8. The 2°×2° resolution permits the resolution of many detailed features of the topography not included by Leichtmann *et al.* In the Northern Hemisphere it can be seen that the sub-arctic gyres are quite suppressed relative to Fig. 4. In the case of the subtropical gyres of the Northern Hemisphere the amplitude is reduced about 30%. The same effect has been noted previously by Sarkisyan and Ivanov (1971). In the Southern Hemisphere, a heavy solid line indicates a transport streamline that marks the center of the most intense flow. It traces the path of what most closely corresponds to the circumpolar current for this case. We note several important differences between the present results in the Southern Ocean and those of Leichtmann *et al.* If we take into consideration the difference in units used in Figs. 7 and 8, we see that the circumpolar current is very much weaker—almost an order of magnitude less. This result is shown in more detail in Table 2. The patterns of mass transport streamfunction corresponding to the first two cases in Table 2 are shown in Figs. 4 and 8, respectively. The remaining cases are based on a smoother field of bottom topography than that shown in Fig. 5, but in other respects they are similar to the second case. No flow patterns are shown for these cases. The first conclusion that one can draw from Table 2 is that topographic barriers in the Drake Passage and at other longitudes greatly reduce the total flow. This reduction of transport by a partial barrier in an idealized model of the Southern Ocean has been noted already by Schulman (1970) and by Bye and Sag (1972) in their companion paper in this issue. Another way to interpret this effect is that relatively few lines of constant $H\csc\varphi$ go through the Drake Passage and circle the earth without being interrupted. There is a strong tendency for absolute vorticity to be conserved unless torques caused by lateral friction, sur-

TABLE 2. Transport of the Antarctic Circumpolar Current (ACC) for a wind-driven, homogeneous ocean.

Bottom topography	A_M ($\times10^8$ cm^2 sec^{-1})	ACC transport ($\times10^6$ tons sec^{-1})
Uniform depth	4	>600
Unsmoothed	4	32
Smoothed	4	24.4
Smoothed	8	21.5
Smoothed	16	19.4
Smoothed	32	18.3

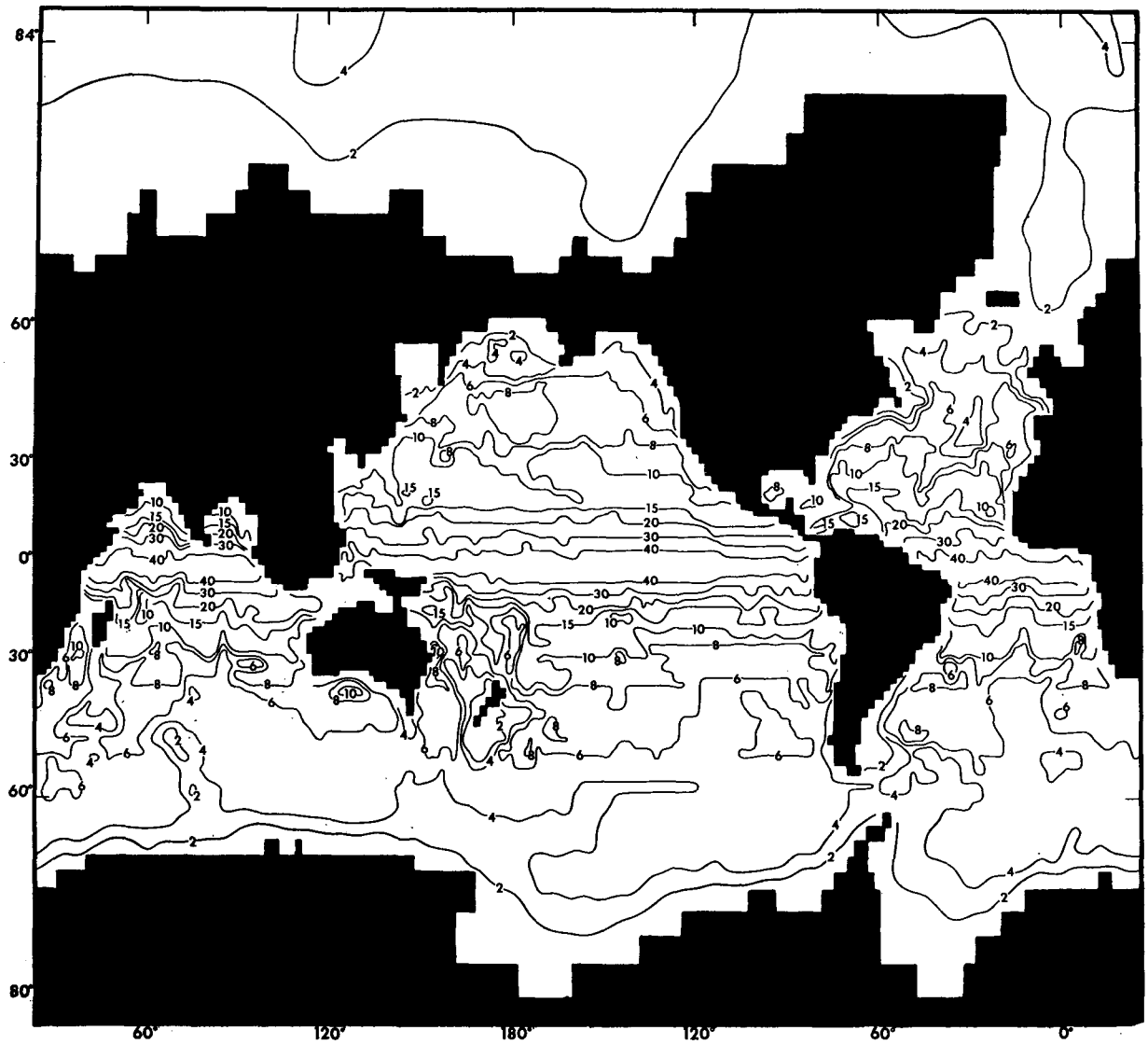

FIG. 6. Lines of $H\csc\varphi$ corresponding to the distribution of depth in the model. Units are 10^3 m.

face stress or inertial effects are present. Since a really large transport through the Drake Passage in this case would require flow to be forced across lines of $H\csc\varphi$, the transport is greatly inhibited by a partial barrier in the passage.

Note that the flow is about 25% less in the smoothed case as compared to the unsmoothed topography for the same level of A_M. Apparently, this difference is due to the fact that the smoothing of the topography tended to fill the Drake Passage and increased the height of the topographic barrier. Comparing the four cases with smoothed bottom topography we see that an eightfold increase in the lateral friction coefficient changes the transport less than 30%. This unexpectedly weak dependence on the value of A_M confirms the prediction of Munk and Palmén (1951) that bottom topography could play a major role in the momentum balance of the circumpolar current.

Other features of the Southern Hemisphere flow pattern in Fig. 8 are the way the flow is guided around the South Pacific Rise at 40S and 120W. The Kerguelen Ridge at 50S and 70E also forces the main axis of zonal flow to make an abrupt excursion poleward. The flow is forced through a relatively narrow gap between the New Zealand Plateau and the Macquarie Ridge which juts out from the Antarctic Continent.

One of the discrepancies between observation and the Stommel-Munk theory of wind-driven ocean circulation is the absence of a steady, powerful western boundary current along the east coast of Australia. The observed East Australian Current is rather weak and variable (Hamon, 1965) in spite of the fact that

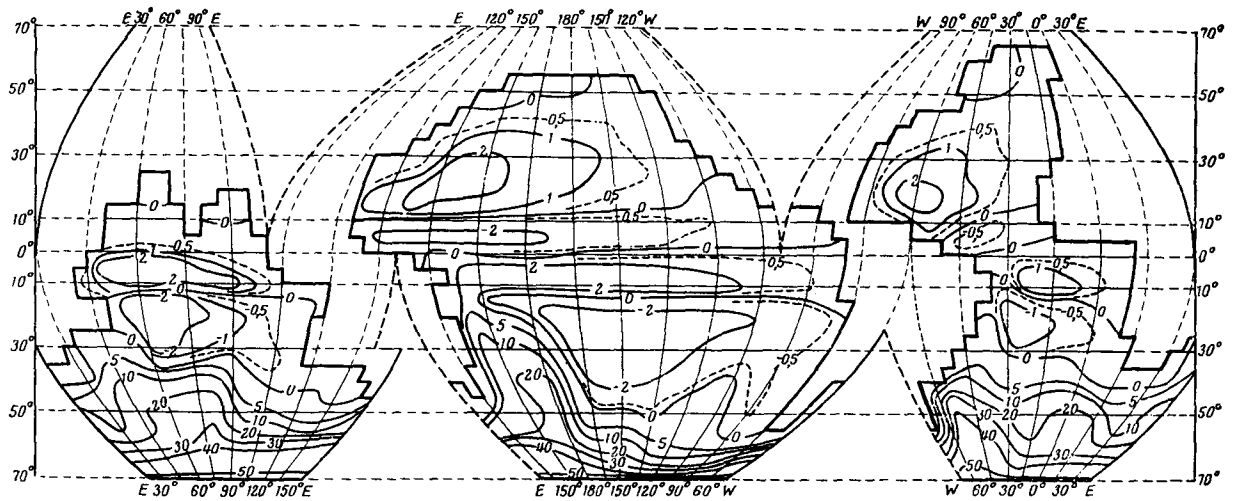

FIG. 7. Transport streamfunction calculated by Leichtmann *et al.* (1971) for realistic bottom topography. Units are 6.37×10^6 tons sec^{-1}.

the subtropical wind gyre in the South Pacific is relatively strong. For the case of uniform depth the numerical calculations of Sag (1969), Il'in *et al.* (1969), and Takano (1969) all predict a strong East Australian Current. This is also true of the pattern shown in Fig. 4 based on the present model. However, the effect of bottom topography shown in Fig. 7 is to completely change the transport pattern in this region. The overall area of the subtropical gyre is reduced by the invasion of the circumpolar current which is deflected northward by the Pacific Rise. More important is the effect of shallow water in the area between the Tonga Islands and Australia which acts as a barrier. A large fraction of the poleward return flow takes place along the edge of this barrier rather than in an intense western boundary current near Australia.

7. Analysis of the vorticity balance

Analysis of the vorticity balance is a familiar tool in dynamic oceanography. It is much better adapted for investigating the flow regime in a limited region than an analysis of the momentum balance. In order to compare the total torque associated with surface wind stresses with the torque exerted by pressure forces acting on the bottom, for example, we must use a vertically *integrated* form of the vorticity equation.

TABLE 3. Definition of various flow regimes based on the two leading terms of the momentum balance.

Regime	Leading terms
I ("Sverdrup")	Wind torque, beta
II ("Munk")	Lateral friction, beta
III ("Equatorial")	Inertial, lateral friction
IV ("Topographic Munk")	Topographic, lateral friction
V ("Topographic Sverdrup")	Wind torque, topographic

Unfortunately, we cannot make use of (17), since that is a vertically *averaged* form.

To derive the vertically integrated form, (15) and (16) must be cross-differentiated; integration by parts then allows us to simplify the pressure terms:

$$\rho_0^{-1}a^{-2}\Delta\psi_t=-\frac{2\Omega}{\rho_0 a^2}\psi_\lambda+\frac{m}{\rho_0 a^2}(H_\varphi p_\lambda-H_\lambda p_\varphi)\Big|_{z=-H}$$
$$-\frac{m^2}{a^2}\left[\int_{-H}^{0}[(uv)_\lambda+(v^2/m)_\varphi]dz\right]_\lambda$$
$$+\frac{1}{a^2}\left[\int_{-H}^{0}m[(u^2)_\lambda+(uv/m)_\varphi]dz\right]_\varphi$$
$$+\frac{mA_V}{a}[V_{\lambda z}-(m^{-1}U_z)_\varphi]_{-H}^{0}$$
$$+\frac{m}{a}\left[\int_{-H}^{0}F^\varphi dz\right]_\lambda-\frac{m}{a}\left[\int_{-H}^{0}m^{-1}F^\lambda dz\right]_\varphi, \quad (32)$$

where F^φ and F^λ are the two components of lateral friction which form the last term of (3) and (4).

The first four terms on the right-hand side are the beta term, the pressure torque acting on bottom topography, and the inertial terms, respectively. Following the inertial terms in (32), the next two terms are the surface and bottom torque due to skin friction. The final term is the torque exerted by lateral friction. In Table 3, several different flow regimes are defined on the basis of the two leading terms of the vorticity balance.

Regime I is the familiar Sverdrup regime of the classical theories of a wind-driven ocean [see Stommel (1958) for a review]. This regime is normally associated

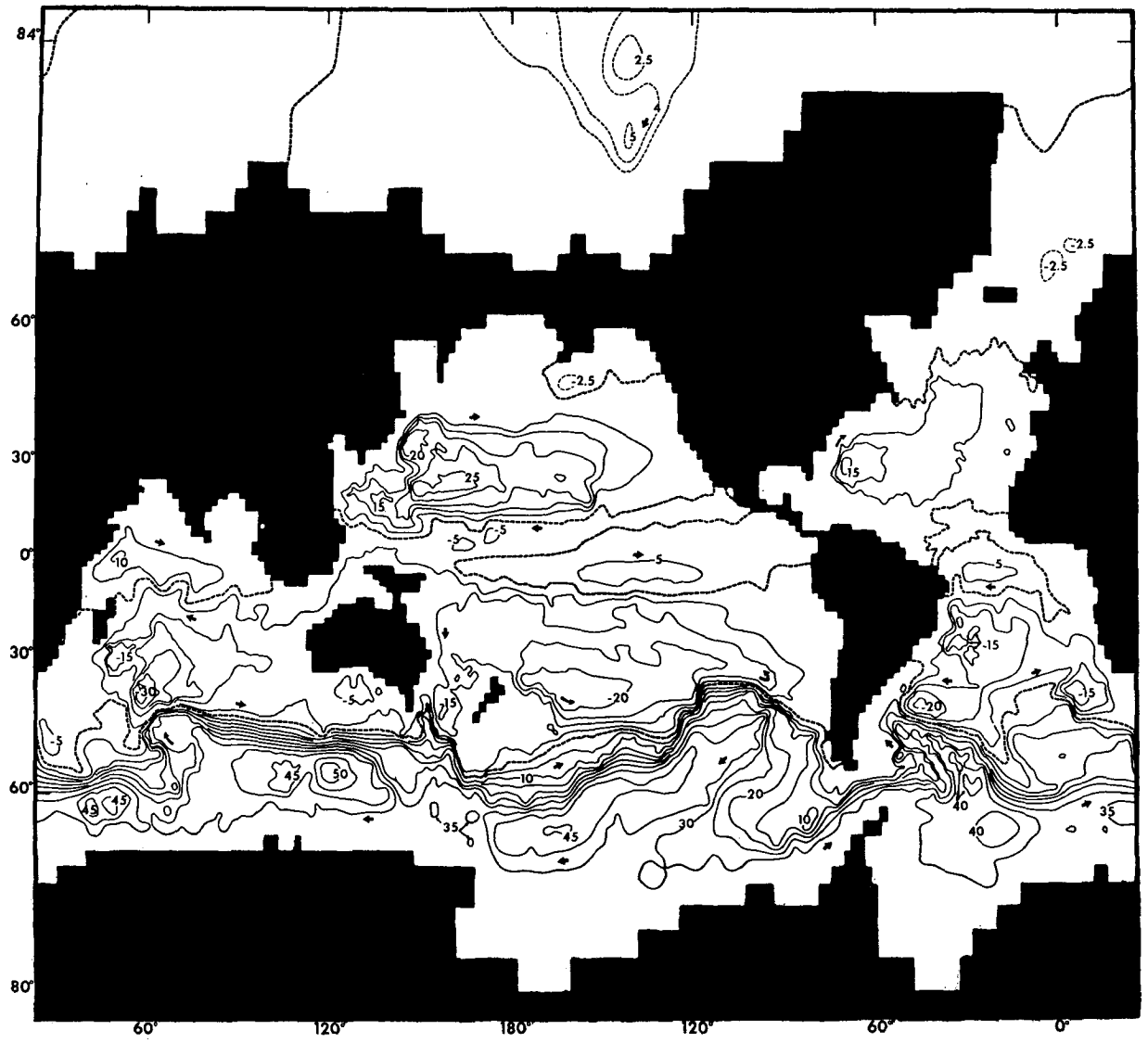

FIG. 8. Pattern of the mass transport streamfunction for the depth configuration shown in Fig. 5. A_M is equal to 4×10^8 cm^2 sec^{-1}.

with the interior region of subtropical and subarctic wind gyres. Regime II is similar to the balance of terms in the western boundary current region of Munk's model of a wind-driven ocean. Regimes III and IV are not ordinarily encountered in wind-driven ocean theory. Regime V, which is analogous to the Sverdrup regime with vortex stretching and shrinking due to flow over topography, plays the same role as the beta effect. This analogy is discussed by Greenspan (1968).

TABLE 4. Percentage of the World Ocean covered by different vorticity balance regimes defined in Table 3. For a regime to exist, the sum of the absolute values of the first two terms must exceed the next largest term by a factor of 3.

	Case	
Regime	Flat bottom	Topography
I	51.1%	20.0%
II	19.4%	16.4%
III	2.4%	2.3%
IV	—	21.5%
V	—	10.1%

One way to analyze the vorticity balance is to look at the total area occupied by each regime. The results are shown in Table 4. The resolution of the grid system ($2°\times2°$) makes it necessary to use a rather large Ekman number (inversely proportional to the Reynolds number). As a result, viscous boundary layers are rather thick and occupy a disproportionately large percentage of the total area. In the "flat bottom" case, the viscous Regime II accounts for 19% of the area. In the case with bottom topography, viscous Regimes II and IV combined, cover about 38% of the total area.

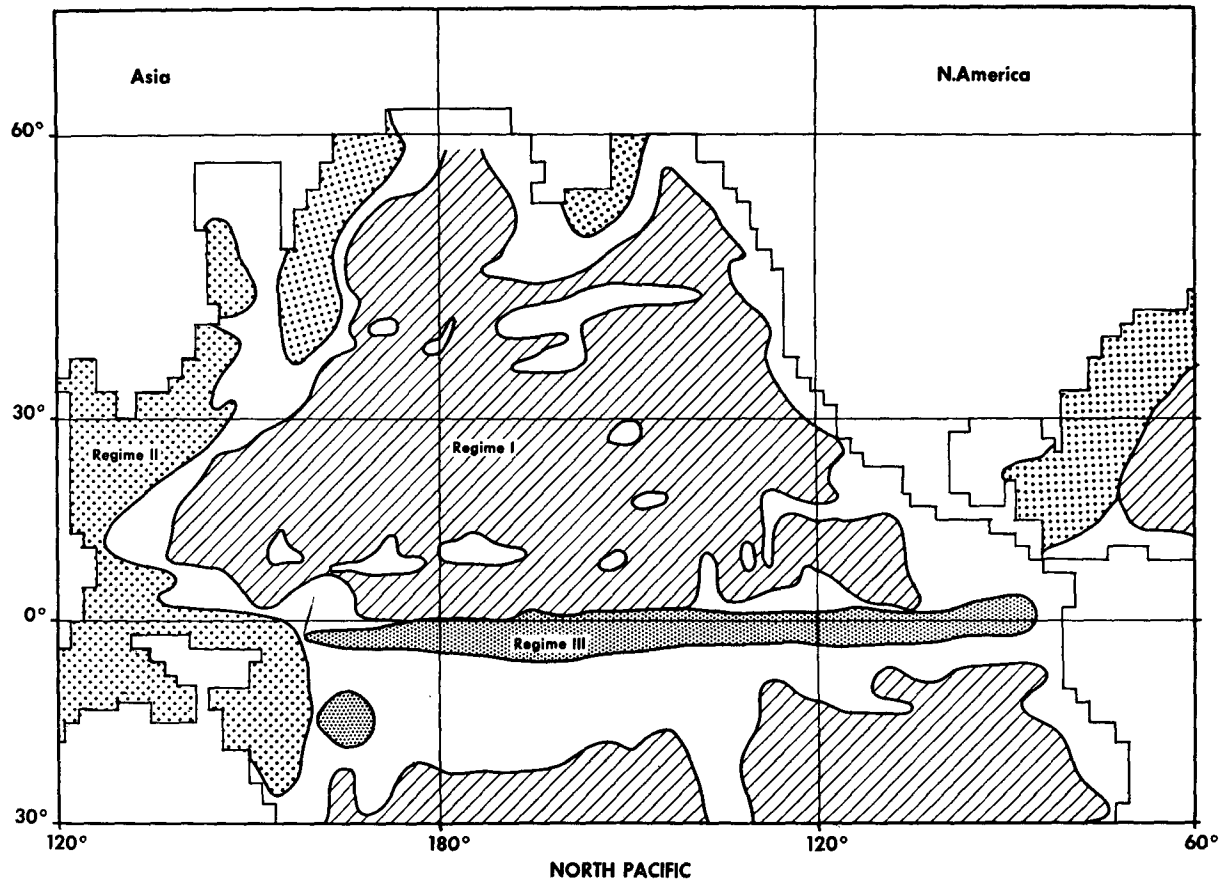

FIG. 9. The vorticity balance in the North Pacific corresponding to the solution shown in Fig. 4. The regimes are defined in Table 3.

In comparing the two cases shown in Table 4 we note that the new topographic Regimes IV and V appear to increase at the expense of the Sverdrup Regime I. In an ideal ocean of uniform density, bottom topography can create intense currents in many interior regions of the ocean basin. As a result, a clear distinction between boundary and interior regimes does not hold for the topographic case. In Part II of this paper we will investigate the extent to which these results are modified in the baroclinic case.

The areas occupied by various flow regimes are quite well defined in the uniform depth case, but tend to be quite broken up when bottom topography is present. With bottom topography there is no clear-cut distinction between viscous boundary layers and interior regions. An example of the uniform depth case is shown in Fig. 9. Only the North Pacific is shown. Note that a Sverdrup (Regime I) balance exists over most of the basin while a viscous planetary boundary current is present on the western boundary. The only unexpected feature is the nonlinear regime along the equator. This feature is directly related to the three-dimensional character of the model. In most of the area of the model, the rotational constraint requires the motion to be two-dimensional except for upper and lower friction boundary layers. Near the equator where the rotational constraint vanishes, inertial effects become important.

8. Discussion

To test a generalized, three-dimensional, time-dependent model of the World Ocean, numerical calculations are carried out for the case of uniform density. The wind-stress field is specified from climatological tables by Hellerman (1967). In the case of uniform depth, the transport patterns calculated for the Northern Hemisphere correspond to what might be predicted from the Stommel-Munk wind-driven ocean theory. In the Southern Hemisphere, the model predicts a transport through the Drake Passage for the uniform depth case exceeding 600×10^6 tons sec^{-1} corresponding to a lateral austausch coefficient of 4×10^8 cm^2 sec^{-1}. Essentially, the results confirm the conclusions of Munk and Palmén (1951) that the Munk model of wind-driven ocean is inadequate to give even a first-order description of the circumpolar current.

The introduction of bottom topography completely

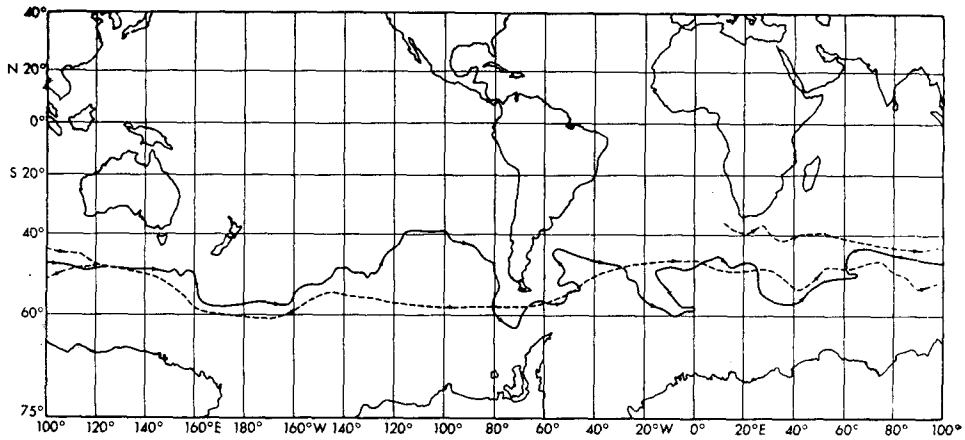

FIG. 10. A comparison of the path of the Antarctic Circumpolar Current (dashed line) estimated by Gordon (personal communication) and the path indicated by the homogeneous model (full line).

changes the transport patterns, particularly in the Southern Hemisphere. In Fig. 10 the path of a transport streamline which best represents the location of the model circumpolar current is compared to the path estimated by A. Gordon[3] (1971) from hydrographic data. If one refers to the pattern of $H\csc\varphi$ given in Fig. 6, it is clear that the model solution is much more influenced by the bottom than the observed pattern. Just upstream and downstream from the Drake Passage, the calculated path of the current makes large meridional excursions which are not indicated in the observed path. Note that the observed current has two branches near Africa and does not rejoin until it reaches the area south of Australia. In a band of longitude from 100E to 140W in the Pacific sector, agreement between the homogeneous model and the observed path is much better. In particular, the model predicts the abrupt poleward shift of the circumpolar current near the Macquarie Ridge south of New Zealand very well. In an earlier study in which topographic features with a scale of less than 1000 km were ignored, Kamenkovich (1962) concluded that a barotropic model was sufficient to account for the major features of the path of the circumpolar current. Except for the good agreement in the western Pacific sector, the present study with more detailed topography leads to the opposite conclusion; i.e., the density distribution of the Southern Ocean must be taken into account to model the observed features of the path of the circumpolar current.

The calculated transport values of the model also indicate the need to consider baroclinic effects. For the case of a flat bottom, the model gives unrealistically large values of transport in the circumpolar current, amounting to over 600×10^6 tons sec^{-1}, even though the viscosity is relatively large. On the other hand, when bottom topography is taken into account, the transport of the circumpolar current drops to less than 30×10^6 tons sec^{-1}. Preliminary results, based on calculations in which the density field is specified from observations, indicate that baroclinic effects raise the transport to $180\text{–}200\times10^6$ tons sec^{-1} which is in much better accord with usual estimates. These calculations will be described in Part II of this study.

Another interesting feature of the solutions is associated with the circulation pattern of the South Pacific. In the case of uniform depth, the solution indicates a very large East Australian Current. The predicted value is almost twice that of the Gulf Stream in the same solution. This result is consistent with the wind-driven ocean theory since the South Pacific subtropical gyre area is nearly twice as wide as the subtropical gyre of the North Atlantic. As pointed out by Stommel (1958) the East Australian Current is actually rather weak compared to the Gulf Stream and this descrepancy is a conspicuous failure of the Stommel-Munk wind-driven ocean theory. Without taking into account baroclinic effects, no final conclusions can be drawn. The solutions, including topography, point to the very important effect of topographic barriers, such as the Tonga Islands, which deflect the westward drift in the model solution causing a diffuse western boundary current rather than a single current at the coast of Australia. The overall effect is to make the Pacific subtropical transport gyre look quite different from the corresponding gyres of the North Atlantic and North Pacific.

Acknowledgments. The authors are very grateful for the assistance they have received from Lt. Cdr. A. J. Semtner, Jr., of the NOAA Officer Corps, and Miss M. B. Jackson and Mrs. J. M. Ferko in carrying out the computations and preparing the manuscript. Discussions with William Holland, Adrian Gill and Arnold Gordon were also extremely helpful. Critical comments by George Philander helped to clarify the relationship between the present results and a much earlier study by Kamenkovich.

[3] Personal Communication.

The calculations were carried out with support made available to NOAA by the National Science Foundation in connection with the International Decade of Ocean Exploration Program.

APPENDIX

Finite-Difference Formulation for the Determination of the Circulation Around Islands

As outlined by Kamenkovich (1962), the treatment of islands in the calculation of the streamfunction is based on splitting the transport streamfunction field into homogeneous and non-homogeneous components, i.e.,

$$\psi^l=\psi_0{}^l+\sum_{r=1}^{R} u_r{}^l\psi_r, \tag{A1}$$

where ψ_0 designates the non-homogeneous part and ψ_r ($r=1, 2, 3 \ldots R$) represents a series of homogeneous fields which are used to satisfy boundary conditions for each island. Let M and N be the vertically averaged acceleration in the λ and φ directions, respectively. Approximating $\partial\psi/\partial t$ by

$$\frac{\partial\psi}{\partial t}\approx(\psi^{l+1}-\psi^{l-1})(2\Delta t)^{-1}, \tag{A2}$$

the equivalent of (17) may be written as

$$[m(\psi_0{}^{l+1}-\psi_0{}^{l-1})_\lambda H^{-1}]_\lambda+[(\psi_0{}^{l+1}-\psi_0{}^{l-1})_\varphi(mH)^{-1}]_\varphi =2\Delta t(N_\lambda-M_\varphi)^l a. \tag{A3}$$

Eq. (A3) is used to predict $\psi_0{}^{l+1}$ with the boundary condition that $\psi_0=0$ on all shore points, including the shores of islands. Although the amplitudes, $\mu_r{}^l$, are a function of time, ψ_r itself can be computed once and held fixed during the time integration; ψ_r is calculated from

$$[m(\psi_r)_\lambda H^{-1}]_\lambda+[(\psi_r)_\varphi(mH)^{-1}]_\varphi=0, \tag{A4}$$

with the condition that ψ_r is zero on all shore points, except along the shore of island r, where it is set equal to unity.

The problem remains as to how $\mu_r{}^l$ is to be determined at each time step. To obtain additional conditions we return to the original equations of motion [(15) and (16)] averaged with respect to the vertical coordinate. These equations are then used to compute the change in circulation around each island, r:

$$\int_r \mathbf{s}\cdot\{\mathbf{k}H^{-1}\times\nabla[\sum_{r=1}^{R}\mu_r{}^{l+1}\psi_r+\psi_0{}^{l+1}-\psi^{l-1}] -2\Delta t(\mathbf{i}M+\mathbf{j}N)^l\}dS=0. \tag{A5}$$

Here $\mathbf{i}$ and $\mathbf{j}$ are the λ and φ components of the horizontal direction vector, and $\mathbf{S}$ is a unit vector parallel to the path of the integral. Since there are R islands, a total of R equations of the form given by (A5) are available to determine $\mu_r{}^{l+1}$ ($r=1, 2, 3 \ldots R$) once $\psi_0{}^{l+1}$, ψ^{l-1}, M^l and N^l are known.

To give some idea what the auxiliary fields corresponding to the homogeneous part of the solution look like, the ψ_r field associated with Australia and Antarctica are shown in Figs. 11a and 11b, respectively. Six "islands" in all are taken into account by the computation. Three correspond to the smaller isolated continents and three to the very largest islands in the World Ocean. Due to the low resolution and rather large Ekman number used in the computation, corresponding to the 2°×2° mesh, circulation through narrow passages and channels is greatly restricted. Therefore, the results would not be improved by including many more islands.

As pointed out in Section 2, the finite-difference formulation given by Bryan (1969) is not consistent for the general case with variable bottom topography. Care must be taken to insure that the finite-difference formulation of (A3), (A4) and (A5) is done in such a way that the finite-difference equivalent of the Stokes circulation theorem is satisfied. Only in that case will the circulation calculated for different islands be independent of the precise path of the circulation integral. In the finite-difference net ψ is defined at $i+\frac{1}{2}$, $j+\frac{1}{2}$ points, while the components of M, N, corresponding to the accelerations of the individual velocity components u and v will be defined at integer values of i and j.

The finite-difference approximation for the vertically averaged equation of motion in the λ and φ directions may then be written

$$D^\lambda{}_{i+\frac{1}{2},j}=(aH)^{-1}\delta_\varphi(\psi_0{}^{l+1}-\psi^{l-1})+2\Delta t\bar{M}^\lambda +(aH)^{-1}\sum_{r=1}^{R}\mu_r{}^{l+1}\delta_\varphi\psi_r, \tag{A6}$$

$$D^\varphi{}_{i,j+\frac{1}{2}}=(aH)^{-1}m\delta_\lambda(\psi_0{}^{l+1}-\psi^{l-1})-2\Delta t\bar{N}^\varphi +(aH)^{-1}\sum_{r=1}^{R}\mu_r{}^{l+1}m\delta_\lambda\psi_r. \tag{A7}$$

The clockwise circulation integral corresponding to (A5) around the outside of a rectangle in i, j space defined by $I<i<I+\Delta I$ and $J<j<J+\Delta J$ is

$$\sum_{i=I}^{I+\Delta I} -am(D^\lambda{}_{i+\frac{1}{2},J+\Delta J}-D^\lambda{}_{i+\frac{1}{2},J})\Delta\lambda +\sum_{i=J}^{J+\Delta J} a(D^\varphi{}_{I,j+\frac{1}{2}}-D^\varphi{}_{I+\Delta I,j+\frac{1}{2}})\Delta\varphi=0. \tag{A8}$$

In many cases the geometry of the World Ocean does not allow a rectangular path to be taken around an island. In that case (A8) can be modified in a straightforward way. With the formulation given by (A6)–(A8)

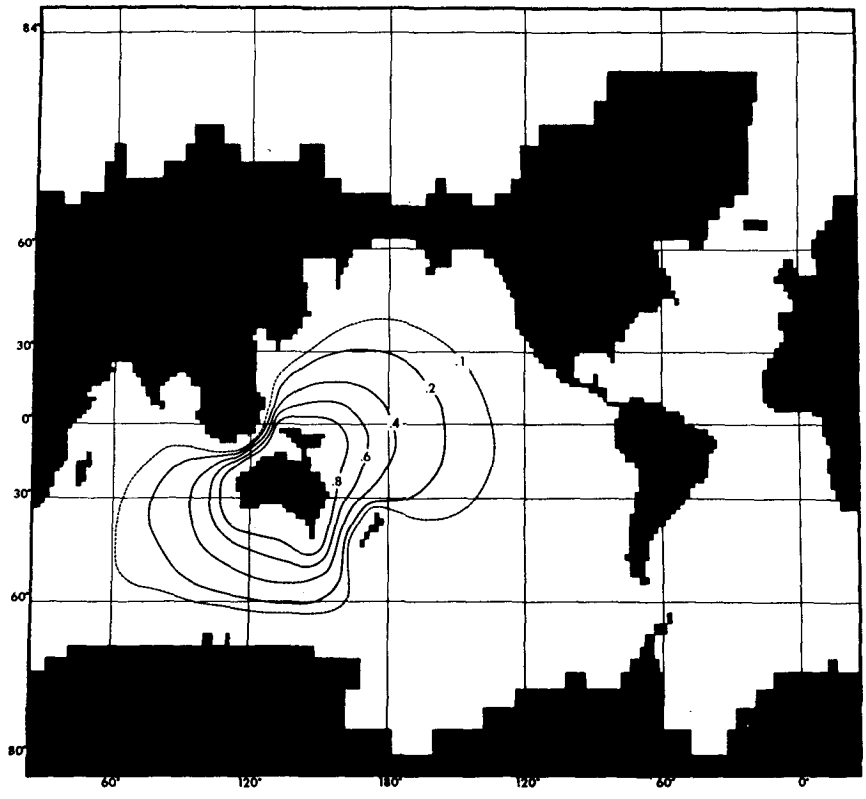

(a)

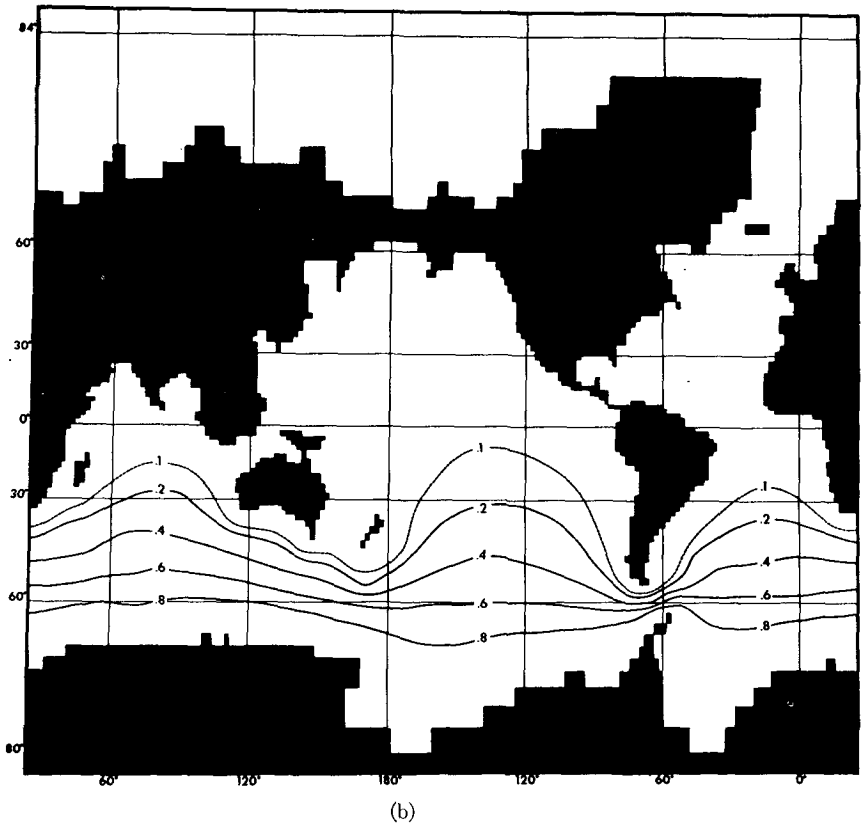

(b)

FIG. 11. Auxiliary fields used in the transport streamfunction computation: (a) for Australia, (b) for Antarctica.

the values of μ_r calculated from several tests were found to be completely independent of the particular part of the circulation integral around the island.

REFERENCES

Allen, D. N. deG., 1954: *Relaxation Methods*. New York, McGraw-Hill, 257 pp.

Bye, J. A. T., and T. W. Sag, 1972: A numerical model for circulation in a homogeneous world ocean. *J. Phys. Oceanogr.*, **2**, 305–318.

Bryan, K., 1969: A numerical method for the study of the circulation of the world ocean. *J. Comput. Phys.*, **3**, 347–376.

——, and M. D. Cox, 1968: A nonlinear model of an ocean driven by wind and differential heating: Parts I and II. *J. Atmos. Sci.*, **25**, 945–978.

Cox, M. D., 1970: A mathematical model of the Indian Ocean. *Deep-Sea Res.*, **17**, 47–75.

Gill, A. E., and R. L. Parker, 1970: Contours of "h cosec ϕ" for the world's oceans. *Deep-Sea Res.*, **17**, 823–824.

Greenspan, H. P., 1968: *The Theory of Rotating Fluids*. Cambridge University Press, 327 pp.

Hamon, B. V., 1965: The East Australian Current, 1960–1964. *Deep-Sea Res.*, **12**, 899–921.

Hellerman, S., 1967: An updated estimate of the wind stress on the world ocean. *Mon. Wea. Rev.*, **95**, 607–626. (Correction, 1968: **96**, 63–74.)

Il'in, A. M., V. M. Kamenkovich, T. G. Zhugrina and M. M. Silkina, 1969: On the calculation of the complete circulation in the world ocean (Stationary problem). *Izv. Atmos. Ocean. Phys.*, **5**, 1160–1171.

Kamenkovich, V. M., 1962: On the theory of the Antarctic Circular Current. *Okeanologiya*, **56**, 245–301.

Lee, W. H. K., and W. M. Kaula, 1967: A spherical harmonic analysis of the earth's topography. *J. Geophys. Res.*, **72**, 753–758.

Leichtmann, D. L., B. A. Kagan, L. A. Oganesian and R. V. Piaskovsky, 1971: On the global circulation of an ocean with variable depth. *Proc. Acad. Sci., USSR*, **198**, 2, 333–336.

Munk, W. H., 1950: On the wind driven ocean circulation. *J. Meteor.*, **7**, 79–93.

——, and E. Palmén, 1951: Note on the dynamics of the Antarctic Circumpolar Current. *Tellus*, **3**, 53–56.

Reid, J. L., and W. D. Nowlin, 1971: Transport of water through the Drake Passage. *Deep-Sea Res.*, **18**, 51–64.

Robinson, A. R., 1970: Boundary layers in ocean circulation models. *Ann. Rev. Fluid Mech.*, **2**, 293–312.

Sag, T. W., 1969: A numerical model for wind-driven circulation of the world's ocean. *Phys. Fluids, Suppl. II*, 177–183.

Sarkisyan, A. S., and F. F. Ivanov, 1971: Joint effect of baroclinicity and bottom relief as an important factor in the dynamics of sea currents. *Izv. Akad. Nauk SSSR, Fiz. Atmos. Okeana*, **1**, 173–188.

Schulman, E. E., 1970: The Antarctic Circumpolar Current. *Proc. Summer Computer Simulation Conf.*, Denver, Colo., 955–968.

Stommel, H., 1958: *The Gulf Stream, a Physical and Dynamical Description*, 2nd ed., 1965. Berkeley, University of California Press, 157 pp.

Takano, K., 1969: General circulation of the world's ocean. *J. Oceangr. Soc. Japan*, **25**, 48–50.